Dalton Transactions

ROYAL SOCIETY OF CHEMISTRY

PAPER

View Article Online
View Journal | View Issue

Check for updates

Cite this: *Dalton Trans.*, 2026, **55**, 1844

Open Access Article. Published on 08 January 2026. Downloaded on 6/2/2026 4:10:33 PM.
This article is licensed under a Creative Commons Attribution 3.0 Unported Licence.

Light- and copper-activated (photo)cytotoxicity of 8-hydroxyquinoline-based boron photosensitizers with lipid droplet targeting and lipid peroxidation accumulation

Thanh Chung Pham,†[a] Gun Kim, †[b] Pham Van Thong,†[c,d] Tran Ngoc Dung,[c] Hung Tan Pham,[a] Nguyen Van Trang,[e] Le Thi Hong Hai,[c] Arne Meulemans,[a] Luc Van Meervelt,[a] Eduard Fron, [a] Mark Van der Auweraer,[a] Daniel Escudero, *[a] Hue Minh Thi Nguyen *[c] and Wim Dehaen *[a]

Received 30th April 2025,
Accepted 8th December 2025

DOI: 10.1039/d5dt01016k

rsc.li/dalton

8-Hydroxyquinoline-based tetracoordinate boron complexes have been observed to exhibit pronounced luminescence and light-activated reactive oxygen species (ROS) generation, while their copper(II) analogs demonstrate significant cytotoxic effects in cancer cells. Nevertheless, both types of complexes are hindered by their inherent hydrophilicity, thereby limiting their efficacy in biological applications. Thus, we developed heavy-metal-free photosensitizers (PSs) based on 8-quinolinolato boron complexes, which exhibit light-activated fluorescence emission and ROS generation upon aggregation. The PSs effectively localize within lipid droplets and exhibit immediate and sustained ROS production upon exposure to light, even under hypoxic conditions, leading to lipid droplet-specific peroxidation, which is in accordance with the intracellular location, leading to ferroptosis-like cell death. Moreover, their fluorescence emission is quenched in the presence of Cu^{2+} ions, and the produced complexes enhance cytotoxicity instead. The photophysical properties of the complexes were comprehensively studied by a combination of experimental measurements, quantum mechanical (QM) and hybrid QM/molecular mechanics (MM) simulations. Thus, this investigation offers insights into new molecular design approaches for multifunctional probes with potential applications in photodynamic therapy and chemotherapy for cancer treatment.

Introduction

Photodynamic therapy (PDT) is recognized as a promising approach for the treatment of various diseases, including cancer, due to its minimal invasiveness and controlled cytotoxicity.[1,2] The procedure involves the administration of photosensitizers (PSs), which are designed to be selectively delivered to and accumulated in tumor tissues.[3–5] Upon specific light irradiation, these PSs produce reactive oxygen species (ROS), which induce the death of malignant cells while sparing the surrounding normal cells. Despite its potential, conventional PSs exhibit several limitations: (1) in their aggregated state, which is common within tumors, their fluorescence emission and ROS generation are significantly quenched.[6,7] (2) The uncontrolled ISC process results in negligible fluorescence radiative decay, limiting their applicability in biological settings.[8,9] (3) While the enhancement of the ISC process can be achieved through the introduction of heavy atoms (*e.g.*, metal complexes, bromine, and iodine), this modification can lead to potential dark cytotoxicity.[10] (4) Most PSs operate *via* a type II photoreaction, which is highly dependent on oxygen concentration.[11–13] This dependence poses a challenge under the hypoxic conditions characteristic of the solid tumor microenvironment.[14,15] (5) PSs often suffer from non-specific localization, reducing the efficacy of the treatment.[16] (6) The limited multifunctionality of PSs restricts their broader application in areas such as synergistic

[a]*Department of Chemistry, KU Leuven, 3001 Leuven, Belgium. E-mail: daniel.escudero@kuleuven.be, wim.dehaen@kuleuven.be*
[b]*Laboratory of Veterinary Pharmacology, College of Veterinary Science and Research Institute for Veterinary Science, Seoul National University, Seoul 08826, Korea*
[c]*Faculty of Chemistry and Center for Computational Science, Hanoi National University of Education, Hanoi, Vietnam. E-mail: hue.nguyen@hnue.edu.vn*
[d]*R&D Center, Vietnam Education and Technology Transfer JSC, Hanoi 100000, Vietnam*
[e]*Institute of Materials Science, Vietnam Academy of Science and Technology, 18 Hoang Quoc Viet, Cau Giay, Hanoi 10000, Vietnam*
†Contributed equally.

This journal is © The Royal Society of Chemistry 2026

Open Access Article. Published on 08 January 2026. Downloaded on 6/2/2026 4:10:33 PM.
This article is licensed under a Creative Commons Attribution 3.0 Unported Licence.

phototherapy, chemosensing, and theranostics.[10] These drawbacks necessitate ongoing research and development to enhance the efficacy and applicability of PSs in clinical settings.[3,10]

Furthermore, PDT triggers a range of cellular responses, ultimately leading to cell death through apoptosis and/or necrosis. However, certain cellular adaptations, such as those induced by hypoxia and the upregulation of multidrug resistance proteins, can render cells resistant to apoptosis.[17,18] This highlights the need for the development of PSs that are minimally dependent on oxygen and capable of inducing non-apoptotic cell death pathways to enhance therapeutic efficacy. Ferroptosis, a form of cell death distinct from apoptosis and characterized by iron dependence and specific morphological changes, including mitochondrial abnormalities and the absence of nuclear responses,[19–21] has recently gained attention as a promising strategy for cancer therapy,[22,23] due to its effectiveness against cancer cells that are resistant to apoptosis.[24] As reported in ref. 24 and 25, ROS generated by PSs lead to the rapid depletion of glutathione (GSH), which subsequently inhibits glutathione peroxidase 4 (GPX4) activity. This inhibition results in the accumulation of lipid peroxides (LPOs), triggering ferroptosis.[24,25]

In a related study, S. Tardito *et al.* demonstrated that 8-hydroxyquinoline induces a dose-dependent reduction in the viability of human tumor cells.[26] However, when copper is co-administered, the ligand's effects are significantly amplified, resulting in substantial cell death across the studied cell lines. Cytotoxic concentrations of 8-hydroxyquinoline-based Cu(II) complexes lead to increased intracellular copper accumulation and extensive vacuolization of the endoplasmic reticulum, preceding a non-apoptotic (paraptotic) form of cell death. Additionally, the detection of heavy metal ions, such as Cu^{2+}, has become a critical focus in bioanalysis and environmental monitoring due to their significant roles in both physiological and pathological processes.[24,27–29] Fluorescent probes have emerged as highly effective tools for detecting Cu^{2+} ions, owing to their advantageous properties, including high selectivity, sensitivity, operational simplicity, rapid response, and low cost.[30–33] Notably, to the best of our knowledge, no studies have yet explored the use of boron complexes containing monoanionic bidentate (N^O) ligands as fluorescent probes for the detection of Cu^{2+}.

Hence, we synthesized a series of 8-hydroxyquinoline-based boron tetradentate complexes (**BQ1–BQ7**). The photophysical properties of these complexes were thoroughly examined in various states, supported by computational studies including density functional theory (DFT) calculations and hybrid QM/MM simulations. Notably, **BQ7** demonstrated significant potential as a heavy-metal-free PS for type I PDT, exhibiting high fluorescence emission under tumor-like conditions, such as in aggregated states and hypoxic environments. **BQ7** was shown to induce lipid droplet-specific peroxidation, leading to ferroptosis-like cell death during PDT. Additionally, **BQ7** functioned as a novel Cu^{2+}-activated probe with enhanced photo-/dark cytotoxicity due to the formation of 8-hydroxyquinoline-based Cu(II) complexes. This design offers a novel type I PS for phototheranostic applications.

Results and discussion

Synthesis and structural characterization

BQ1–BQ7 were synthesized through a straightforward reaction between BPh_3 and 8-hydroxyquinoline derivatives at ambient temperature using a 1 : 1 molar ratio of BPh_3 to ligand in chloroform solvent (Scheme 1). The structures of **BQ1–BQ7** were confirmed by NMR, HR-MS, and IR spectroscopy and elemental analysis (MAD = 0.09–0.23%), and the details are presented in the SI. To further explore the structures of the complexes, three representative complexes including **BQ2**, **BQ6** and **BQ7** were studied by single-crystal X-ray diffraction (SC-XRD). The molecular structures of **BQ2**, **BQ6** and **BQ7**, as shown in Fig. 1, confirm that the

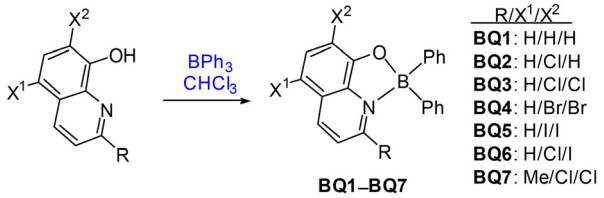

Scheme 1 Preparation of boron(III) complexes **BQ1–BQ7**.

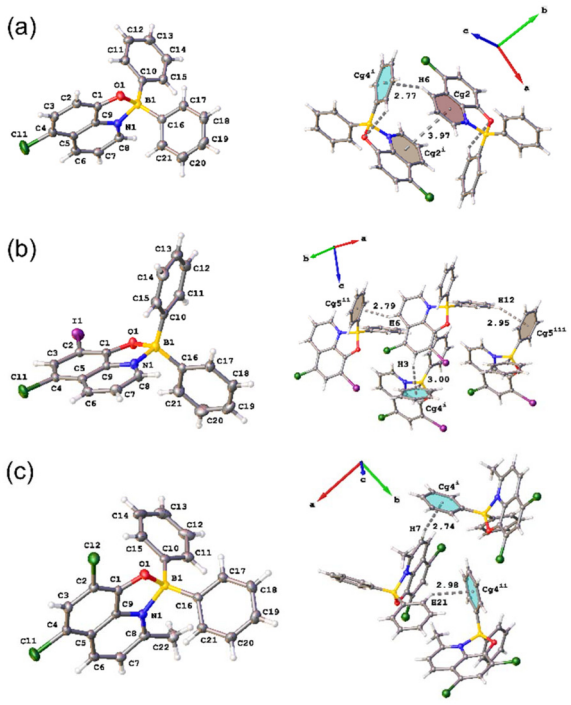

Fig. 1 The molecular structures and partial crystal packing of **BQ2** (a), **BQ6** (b) and **BQ7** (c). Relevant geometrical parameters (in Angstroms) for the most important intermolecular interactions in the crystal structures are highlighted and further analyzed in the SI.

Open Access Article. Published on 08 January 2026. Downloaded on 6/2/2026 4:10:33 PM.
This article is licensed under a Creative Commons Attribution 3.0 Unported Licence.

boron center in these complexes exhibits a typical tetrahedral coordination with two carbon atoms of the phenyl groups and with the N and O atoms of the quinolinolate ligand. Furthermore, the powder XRD pattern calculated from the SC-XRD structure of **BQ7** (Fig. S44c) exhibits strong agreement with the corresponding experimental pattern. In contrast, the discrepancies observed between the calculated and experimental powder XRD patterns for **BQ2** and **BQ6** (Fig. S44a and S44b, respectively) are appreciable rather than marginal. These divergences indicate the presence of multiple crystalline phases: one consistent with the structure determined by single-crystal analysis and another phase responsible for the significantly more intense diffraction peaks observed in the experimental data.

Photophysical characteristics

Investigation of the steady-state absorption and emission spectra of **BQ1–BQ7** compounds was conducted in different solvents, *i.e.*, from non-polar (*e.g.*, toluene (Tol)) to aprotic polar (*e.g.*, tetrahydrofuran (THF) and acetonitrile (ACN)) ones at 10 μM concentration (Fig. 2a, S1 and S2). Notably, the UV-vis absorption band peak between 386 and 421 nm in these solvents indicates the presence of boron-chelated 8-hydroxyquinoline moieties. For all compounds, the absorption bands are structureless. Additionally, these compounds demonstrate a modest hypsochromic shift in absorption with an unchanged emission peak as solvent polarity increases. Attribution of the hypsochromic shift to a decreased polarizability is less likely, as the hypsochromic shift of the absorption maxima is not paralleled by a similar shift in the emission spectra (*vide infra*).[34] The unsubstituted **BQ1** compound exhibited an absorption band maximum ranging from 386 to 400 nm with a prominent emission band maximum at approximately 502 nm (fluorescence quantum yield, FL QY (Φ_F) = 0.41–0.62) in Tol, THF, and ACN. In analogy to its corresponding absorption spectra, the emission bands are structureless. The series of halogen-substituted compounds (**BQ2–BQ6**) exhibited similar features and a discernible bathochromic shift in their absorption and emission spectra when compared to **BQ1** (Table 1). They showed similar Stokes shifts of about 5000 cm^{-1}, which are much larger than the values observed for BODIPY[34] or cyanine dyes, indicating significant changes in bond lengths or angles upon excitation. The red shift of the spectra of **BQ2–BQ6** compared to **BQ1** can be attributed to the electron-withdrawing nature of the halogen substituents, resulting primarily in a decrease in the energy of the lowest unoccupied molecular orbital (LUMO), consequently reducing the highest occupied molecular orbital (HOMO)–LUMO energy gap. The FL QYs and fluorescence decay times of **BQ2–BQ6** are decreased as compared to those of **BQ1**, and this trend is particularly evident in the cases of **BQ4** and **BQ6**. This decrease can mainly be attributed to the enhanced intersystem crossing (ISC) processes induced by the heavy-atom effect which is most marked for the compounds bearing iodine atoms. One should note that the decrease in the FL QY is more marked than that in the FL decay time, suggesting a decrease in the FL rate constant by 40 ± 10%. Of particular interest is **BQ7**, where the introduction of a methyl group led to a higher emission QY as compared to that of **BQ3**.

Motivated by the observed reduction in fluorescence emission in **BQ4–6**, which has been putatively assigned to efficient ISC processes in the latter compounds, the singlet oxygen ($^1O_2$) QYs of all compounds were measured in ACN employing $Ru(bpy)_3^{2+}$ as a reference (see the results in Table 1). Notably, **BQ5** and **BQ6**, characterized by the presence of iodine atoms, demonstrated the highest efficiencies for $^1O_2$ generation ($^1O_2$ QY, Φ_Δ = 0.43 and Φ_Δ = 0.42, respectively, see Table 1). Incorporation of two bromine atoms into the molecular scaffold (**BQ4**) leads to a lower $^1O_2$ QY (Φ_Δ = 0.28). Intriguingly, boron complexes devoid of heavy atoms (**BQ1–3,7**) also displayed non-negligible singlet oxygen generation. This suggests that non-radiative decay in these compounds occurs at least partially by ISC.

Further comprehensive photophysical characterization of **BQ1–BQ7** was conducted in condensed phases, including Zeonex film (5% doping), the solid-state, and organic glass matrices (in Tol at 77 K) (Fig. S1–S4). The absorption and emission spectra of **BQ1–BQ7** in films (Fig. 2c) exhibited a discernible bathochromic shift compared to their respective spectra in the solution phase (see Tables 1 and 2). Conversely, the emission peaks experienced a hypochromic shift in the solid state (Fig. 2c) and in organic glass environments (*e.g.*, Tol, THF, and ACN at 77 K, see Fig. S1 and S2).

To gain deeper insights into the fluorescence emission behavior of **BQ1–BQ7**, excited-state lifetimes were recorded with time-correlated single-photon counting (TCSPC) in solvents, films and solid states (Fig. S1–S4). In Tol at 10 μM concentration, **BQ1–BQ4**, and **BQ7** exhibited single-component emission profiles characterized by prolonged fluorescence lifetimes (with values ranging between 10.0 and 24.3 ns, see Table 1). Conversely, **BQ5** and **BQ6** exhibited emissions with dual components of monomer and aggregate emission. Notably, the emissions of **BQ1–BQ7** in films and solid-state environments exhibited dual components, also suggestive of monomer and aggregate emissions (Tables 2 and S2).

To examine the emission in the aggregated state, the emission characteristics of **BQ7** were investigated in THF with distilled water (DW) (0–99%) (Fig. 2d and S7). The emission peak shifted from 528 (at 0% DW) to 520 nm (at 99% DW), accompanied by a substantial enhancement in intensity (~5 times) at 99% DW. Furthermore, the singlet oxygen ($^1O_2$) and superoxide radical oxygen ($O_2^{\bullet-}$) generation of **BQ7** were assessed in the aggregated state (at THF/DW (5/95)) utilizing 1,3-diphenylisobenzofuran (DPBF) and dihydroethidium (DHE) as probes (Fig. 2e and f, respect-

 This journal is © The Royal Society of Chemistry 2026

Open Access Article. Published on 08 January 2026. Downloaded on 6/2/2026 4:10:33 PM.
This article is licensed under a Creative Commons Attribution 3.0 Unported Licence.

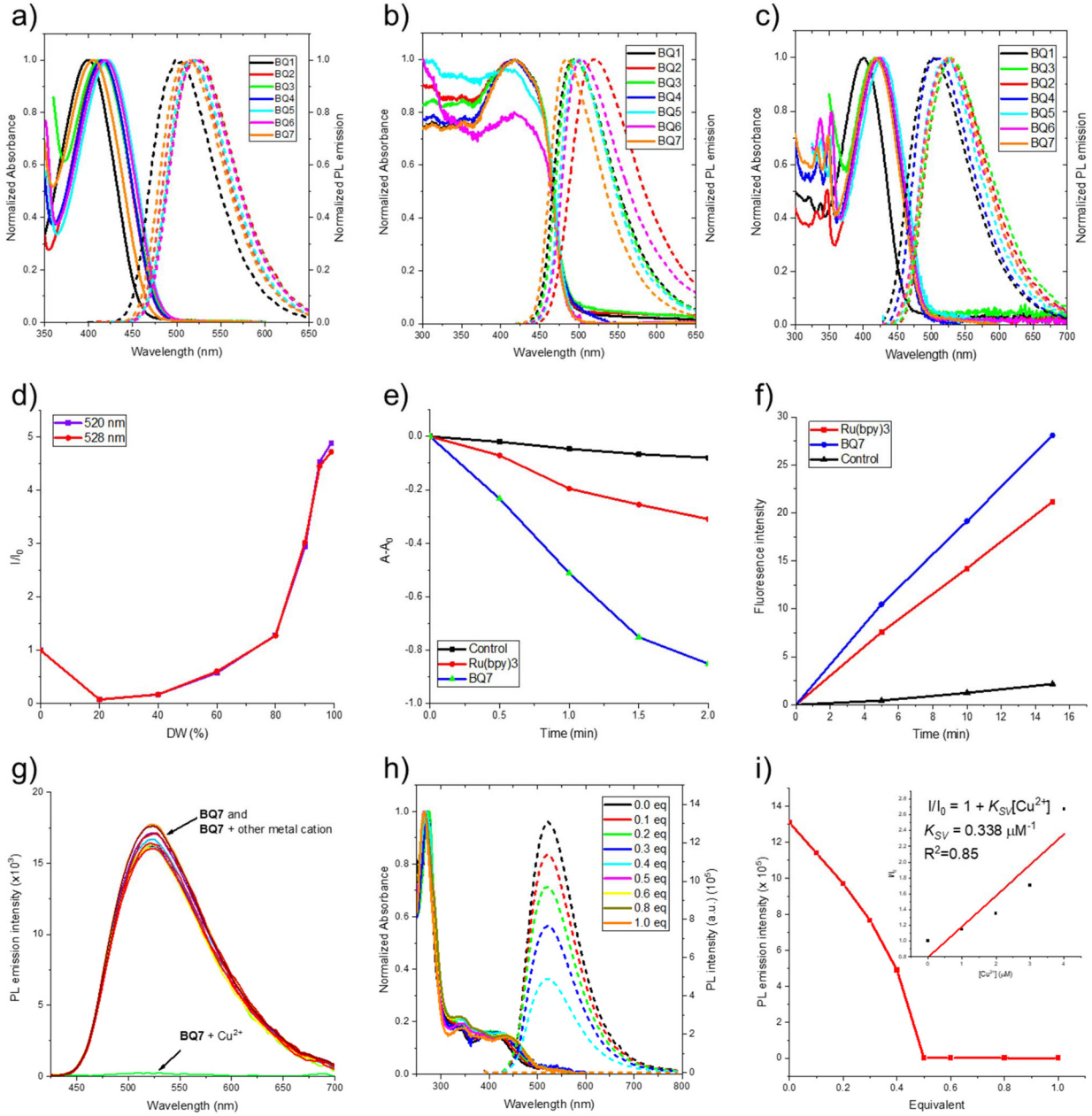

Fig. 2 Normalized absorption (solid lines) and PL emission (dashed lines) spectra of **BQ1–BQ7** in (a) toluene (10 μM, λ_{ex} = 390–410 nm), (b) solid state, and (c) film; (d) fluorescence intensity ratio (I/I_0) of **BQ7** in THF/DW (0–99%); (e) absorbance decrease of 1,3-diphenylisobenzofuran (DPBF) in the presence of PSs (*e.g.*, **BQ7** and $Ru(bpy)_3$) in THF/DW (5/95) under light irradiation; (f) the fluorescence intensity of dihydroethidium (DHE) in the presence and absence (as a control group) of PSs in THF/DW (5/95) under light irradiation; (g) fluorescence emission of **BQ7** (10 μM) in the presence of metal cations (10.0 eq.) in THF/DW (5/95); (h) UV-vis absorption and fluorescence emission spectra of **BQ7** (10 μM) in the presence of Cu^{2+} (0–1.0 eq.) in THF/DW (5/95); (i) fluorescence intensity of **BQ7** (10 μM) in the presence of Cu^{2+} (0–1.0 eq.) in THF/DW (5/95) (the Stern–Volmer constant (K_{SV})-dependent fluorescence intensity ratio (I/I_0) is provided in the inset).

ively). Intriguingly, the decrease in DPBF absorption and the increase in DHE intensity observed in the presence of **BQ7** surpassed those of $Ru(bpy)_3^{2+}$ at the same absorbance under light irradiation, indicating efficient ISC processes and consequent ROS generation. Thus, **BQ7** demonstrates significant potential as an effective PS for fluorescence imaging-guided PDT.

Sensing of Cu^{2+} with BQ7

In the literature, metal complexes derived from 8-hydroxyquinoline (Q)-based ligands have garnered considerable attention owing to their broad utility in luminescence materials and biological applications and are typically synthesized *via* direct reaction of 8-hydroxyquinoline. Here, we explore the feasibility

Open Access Article. Published on 08 January 2026. Downloaded on 6/2/2026 4:10:33 PM.
This article is licensed under a Creative Commons Attribution 3.0 Unported Licence.

Table 1 Photophysical properties of **BQ1–BQ7** in solvents. Absorption maxima (λ_{max}), emission maxima (λ_{em}), molar absorption coefficient (ε), fluorescence QY (Φ_F) and relative singlet oxygen QY (Φ_Δ)

	λ_{abs} (nm)/ε (M^{-1} cm^{-1}) ($\times 10^3$)			λ_{ems} (nm)/Φ_F			τ_F (ns)	Φ_Δ
Sol.	Tol	THF	ACN	Tol	THF	ACN	Tol	ACN
BQ1	400/2.92	393/2.42	386/2.82	500/0.59	502/0.62	502/0.41	24.3	0.15
BQ2	414/3.30	408/2.68	401/3.29	522/0.17	522/0.15	522/0.13	17.2	0.14
BQ3	412/1.32	400/1.63	395/1.48	522/0.20	522/0.09	522/0.08	14.5	0.14
BQ4	415/2.88	406/2.67	401/3.17	519/0.15	519/0.13	519/0.10	10.0	0.28
BQ5	421/2.94	414/3.34	407/3.51	521/0.03	519/0.02	521/0.02	1.8/4.7	0.43
BQ6	419/3.08	412/2.68	403/3.21	528/0.06	528/0.04	528/0.04	4.4/13.7	0.42
BQ7	405/2.47	397/1.94	389/2.77	516/0.41	514/0.32	514/0.26	23.3	0.16

Table 2 Photophysical properties of **BQ1–BQ7** in film and solid states. Absorption maxima (λ_{max}), emission maxima (λ_{em}), and fluorescence QY (Φ_F)

	λ_{abs} (nm)	λ_{ems} (nm)/Φ_F			τ_F [a] (ns)	
	Film	Tol 77 K	Film	Solid	Film	Solid
BQ1	400	484/—	501/0.45	493/0.32	20.8	23.5
BQ2	420	496/—	529/0.40	520/0.19	18.8	12.3
BQ3	421	484/—	530/0.30	491/0.18	20.1	16.5
BQ4	421	449/—	508/0.15	484/0.02	8.0	5.6
BQ5	426	507/—	526/0.03	498/0.01	5.2	1.2
BQ6	426	506/—	529/0.08	503/0.03	4.6	2.6
BQ7	409	498/—	524/0.31	494/0.31	22.6	16.1

[a] Average τ_F, – not recorded.

of 8-hydroxyquinoline-based boron complexes transforming into their corresponding metal complexes and their potential use in sensing applications. To this end, **BQ1–7** (10 μM) were chosen for reaction with various metal cations, including Co^{2+}, Ni^{2+}, Fe^{3+}, Cd^{2+}, Cu^{2+}, Al^{3+}, Cr^{3+}, Zn^{2+}, Pb^{2+}, and Mn^{2+} (10.0 eq.) in DW containing 5% THF. Intriguingly, upon introduction of Cu^{2+}, a substantial quenching of the fluorescence emission of **BQ7** was observed, as evidenced both by spectral analysis (Fig. 2g) and under 365 nm light irradiation (Fig. S8). Conversely, negligible perturbation of the emission profile of **BQ7** was observed upon addition of other metal cations (Fig. 2g). In addition, no differences in the fluorescence emission of **BQ1–BQ6** in the presence of metal cations including Cu^{2+} were observed (Fig. S9), indicating the selective sensing of **BQ7**. Subsequently, titration experiments were conducted to elucidate the interaction between **BQ7** and Cu^{2+}, revealing a gradual decrease in emission intensity culminating in complete quenching at 0.5 eq. of Cu^{2+} (Fig. 2h, 2i and S10). The Stern–Volmer constant (K_{SV}) and the bimolecular quenching rate constant (k_q) were calculated to be 0.34×10^{-6} M and 41.2 M^{-1} s^{-1}, respectively. This observation suggests the formation of non-luminescent copper complexes, specifically denoted as **$(Q7)_2Cu$** (see Fig. 3a). To corroborate this hypothesis, further titration experiments were undertaken employing ^{1}H-NMR spectroscopy in acetone-d_6. These investigations revealed a concomitant decrease and increase in proton intensities corresponding to **BQ7** and chlorodiphenylborane, respectively.

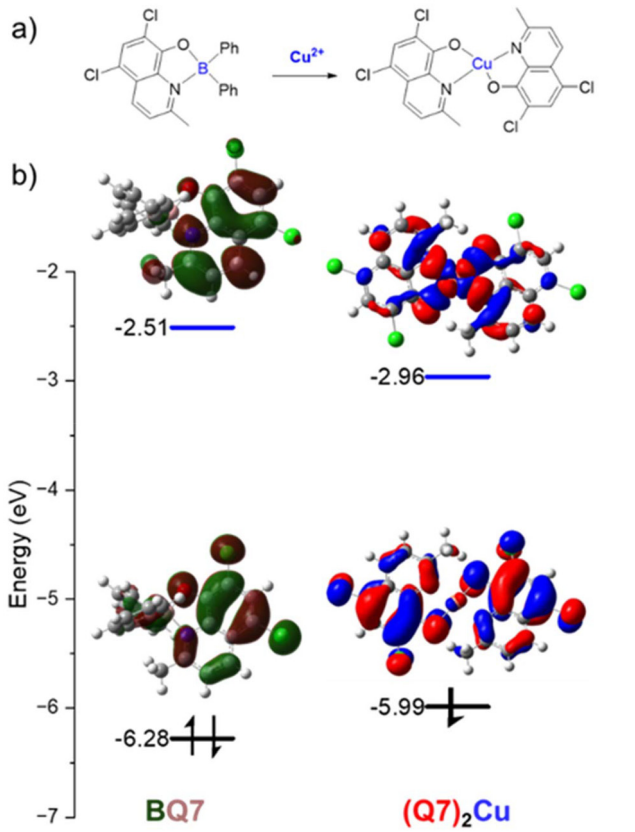

Fig. 3 (a) Proposed sensing mechanism of **BQ7** with Cu^{2+}; (b) frontier molecular orbital images and energies of **BQ7** and **$(Q7)_2Cu$** at optimized S_0 geometries by using MPW1PW91/6-31+g(d,p) level theory in PCM (with Tol as solvent).

The latter is a byproduct generated in the reaction of **BQ7** with $CuCl_2$ (Fig. S11). Notably, while the signal corresponding to **$(Q7)_2Cu$** could not be observed in its doublet form, its presence was further substantiated through mass spectrometric analysis of **BQ7** after the addition of Cu^{2+} (at 0.2 eq.) (Fig. S12). Significantly, the observed "on–off" emission of **BQ7** upon interaction with Cu^{2+} in the aggregated state underscores its potential utility as a chemosensor and phototheranostic probe, thereby holding promise for diverse biological applications.

This journal is © The Royal Society of Chemistry 2026

Open Access Article. Published on 08 January 2026. Downloaded on 6/2/2026 4:10:33 PM. This article is licensed under a Creative Commons Attribution 3.0 Unported Licence.

Computational studies

Encouraged by the intriguing photophysical properties of **BQ7** in the aggregated state and its sensing capabilities, quantum chemical calculations on the **BQ** series were performed. The geometries of the ground (S_0) and lowest singlet (S_1) excited states of the **BQ** series were optimized using density functional theory (DFT)[35] and time-dependent DFT (TD-DFT)[36] with the Tamm–Dancoff approximation (TDA)[37] (see details of the computational protocol in the SI), respectively. The absorption and emission spectra of the **BQ** derivatives, peaking at 400–420 nm and 500–530 nm, respectively, were attributed to the $S_0 \rightarrow S_1$ and $S_1 \rightarrow S_0$ electronic transitions, which mainly involve HOMO and LUMO (see Tables S4 and S5). The HOMO and LUMO are predominantly localized on the quinoline ligand and the central boron atom, with minimal contributions from the phenyl ligands (Fig. S13), confirming the local excitation (^{1}LE) character of S_1. Additionally, the geometry of the **(Q7)$_2$Cu** complex was optimized. The ground state of the **(Q7)$_2$Cu** complex corresponds to a doublet state, *i.e.*, D_1. Analysis of the frontier molecular orbitals of **(Q7)$_2$Cu** reveals that the singly occupied molecular orbital (SOMO) is primarily located on the quinoline ligand, where the LUMO is distributed over the quinoline ligand and the central copper atom (Fig. 3b). The D_1 of **(Q7)$_2$Cu** is indeed of ^{2}LMCT character. ^{2}LMCT states are often involved in efficient non-radiative deactivation channels, outcompeting fluorescence or phosphorescence, and thus leading to the quenching of emission.[38] Furthermore, Cu(II) complexes experience Jahn–Teller distortions,[39,40] especially in octahedral or distorted tetrahedral geometries. This distortion leads to a non-rigid structure, increasing non-radiative relaxation pathways through structural changes in solvents, further quenching emission.[41] The optimal geometries of the T_1 and T_2 triplet excited states of the **BQ** series were also optimized by the TDA TD-DFT method.[35,37] The calculated adiabatic energy differences with respect to S_0 are shown in Table 3. The energy of S_1 is significantly higher than that of T_1 and lower than that of T_2, indicating that the most likely ISC pathway is the S_1–T_1 transition. The ISC rate constant (k_{ISC}) depends mainly on the energy gap and the spin–orbit couplings (SOCs) between the involved singlet and triplet excited states.[42,43] For the **BQ1–BQ7** series, S_1 and T_1 are relatively close in energy. The computed SOCs between the S_1 and T_1 states of **BQ1–BQ7** are also presented in Table 3. While chlorination does not significantly impact the calculated SOC values (0.07–0.09 cm^{-1}), bromine and iodine substitution significantly increase the computed SOCs, attributable to the heavy-atom effect, such as, the diiodo-substituted **BQ5** (0.64 cm^{-1}), dibromo-substituted **BQ4** (0.18 cm^{-1}) and mono-iodo-substituted **BQ6** (0.46 cm^{-1}). Consequently, **BQ5** possesses the highest Φ_Δ value, while **BQ2**, **BQ3**, and **BQ7** possess nearly identical Φ_Δ values to that of **BQ1**. These computational results qualitatively agree with the experimental pieces of evidence.

In addition, SOCs are not the sole factor influencing ISC rates. To achieve more quantitative agreement, the excited state decay rate constants were calculated. The ISC rate constant for the $S_1 \rightarrow T_1$ transition was calculated with the Franck–Condon (FC) approximation but also including Herzberg–Teller (HT) effects[44] (see the results and a comparison of both approaches in Table 3). The calculated ISC rate constants for **BQ1–7** are likely underestimated due to the neglect of HT effects within our theoretical approach. Not surprisingly, **BQ5** possesses the largest ISC rate constant (3.7×10^8 s^{-1}), higher than those of **BQ4** and **BQ6**, and significantly greater than those of **BQ1–3** and **BQ7**. Their S_1–T_1 energy gaps are comparable; therefore, the lower ISC rate constants observed for **BQ1–3** and **BQ7** are primarily attributed to the smaller SOC between the S_1 and T_1 states.

Furthermore, ISC rates are not the only factor impacting fluorescence emission. To obtain a more quantitative agreement of Φ_F, the fluorescence rate constant (k_{fl}) for the $S_1 \rightarrow S_0$ transition was also calculated using the FC/HT approximation. Under the assumption that the nonradiative mechanisms are dominated by the $S_1 \rightarrow T_1$ ISC processes, the FL QY can be expressed using the following equation:

$$\Phi_{fl} = \frac{k_{fl}}{k_{fl} + k_{ISC}} \quad (1)$$

Using eqn (1), there is a qualitative/semi-quantitative good agreement between the calculated and experimental FL QYs, with high values for **BQ1–3** and **BQ7** and the lowest values for **BQ4–6** (see Tables 1 and 3). For example, the experimental and computed FL QY values for **BQ1**, **BQ5** and **BQ7** are 0.62 and

Table 3 Calculated excited state properties of **BQ1–BQ7**. The singlet and triplet excited states were optimized by the TDA TD-DFT method using MPW1PW91/6-31+g(d,p) in PCM (Tol as solvent). Adiabatic energy difference with respect to the optimized S_0 energies (E_{ad}), singlet–triplet energy gaps (ΔE_{S-T}), spin–orbit couplings (SOCs), ISC rate (k_{ISC}), fluorescence rate (k_{fl}), and computed fluorescence QYs (Φ_{fl})

	E_{ad} (eV)			S_1–T_1				S_1–S_0	
	S_1	T_1	T_2	ΔE_{S-T} (eV)	SOCs (cm^{-1})	k_{ISC} (s^{-1}) (FC-HT)	k_{ISC} (s^{-1}) (FC)	k_{fl} (s^{-1})	Φ_{fl} (cal.)
BQ1	2.62	1.58	3.14	1.04	0.09	6.9×10^6	4.8×10^5	1.0×10^7	0.59
BQ2	2.49	1.48	3.00	1.01	0.09	6.8×10^6	4.2×10^5	1.1×10^7	0.62
BQ3	2.49	1.50	2.30	0.99	0.10	1.8×10^6	3.5×10^4	3.7×10^6	0.67
BQ4	2.48	1.52	2.98	0.96	0.18	1.6×10^8	5.0×10^5	7.9×10^6	0.05
BQ5	2.48	1.54	2.70	0.94	0.64	3.7×10^8	9.8×10^5	8.9×10^6	0.01
BQ6	2.47	1.50	2.70	0.97	0.46	1.1×10^8	9.6×10^5	4.2×10^6	0.02
BQ7	2.52	1.54	3.00	0.98	0.07	5.3×10^6	6.0×10^4	2.5×10^6	0.32

Open Access Article. Published on 08 January 2026. Downloaded on 6/2/2026 4:10:33 PM.
This article is licensed under a Creative Commons Attribution 3.0 Unported Licence.

0.59, 0.03 and 0.01, and 0.41 and 0.32, respectively. This confirms the relevance of heavy-atom and vibronic Herzberg–Teller effects in determining the ISC and fluorescence rate constants of PSs.

Motivated by the enhanced fluorescence emission and ROS generation of **BQ7** in its aggregated state, which can be induced by the interactions of **BQ7** with its neighboring molecules (*e.g.*, dimers, trimers, and tetramers),[7] we conducted QM/MM simulations using a multilayer ONIOM model in PCM (water).[45] In its crystalline form, we observed that **BQ7** exhibits π–π stacking interactions between the quinoline and phenyl groups of two molecules (Fig. S15c), which are believed to be the main π–π interaction between them. Consequently, these two molecules (**BQ7** dimer) were designated as the QM layer in the QM/MM calculations, while the surrounding molecules were treated as the MM layer (see Fig. 4a). The departing molecular structure for the QM/MM optimizations was extracted from the crystalline data. The geometries of the first singlet (S_1) and triplet (T_1) excited states were optimized with QM/MM (see details in the SI). At the Franck–Condon geometry, the $S_1 \rightarrow S_0$ and $T_1 \rightarrow S_0$ transitions were predominantly (>96.6%) attributed to the HOMO–LUMO transition, where the HOMO and LUMO are localized on the same molecule (see Fig. 4a and S16), indicating ^{1}LE and ^{3}LE character for the lowest singlet and triplet excited states of the **BQ7** dimer, respectively. Notably, the oscillator strength of S_1 in the **BQ7** dimer (f = 0.12) is larger than that of the monomer (f = 0.07), confirming the enhanced emission of **BQ7** upon aggregation, which can be induced by interaction of **BQ7** with its neighboring molecules (Fig. 4b). In addition, the singlet–triplet adiabatic energy gap between S_1 and T_1 in the **BQ7** dimer was calculated to be 0.78 eV, which is lower than that of the monomer state (0.98 eV) (Fig. 4b). The SOC between S_1 and T_1 was computed to be 0.13 cm^{-1} in the dimer, while those in the monomer are remarkably smaller (0.07 cm^{-1}) (see Fig. 4b). Note that the ISC rate constant (k_{ISC}) is proportional to the SOC and inversely proportional to the energy gap between the singlet and triplet states. This indicates that the efficient ISC process of **BQ7** in the dimer state can be ascribed to an aggregation-induced ISC (AI-ISC) mechanism,[7] which is beneficial for ROS generation *via* both type I and type II mechanisms in its aggregated states.

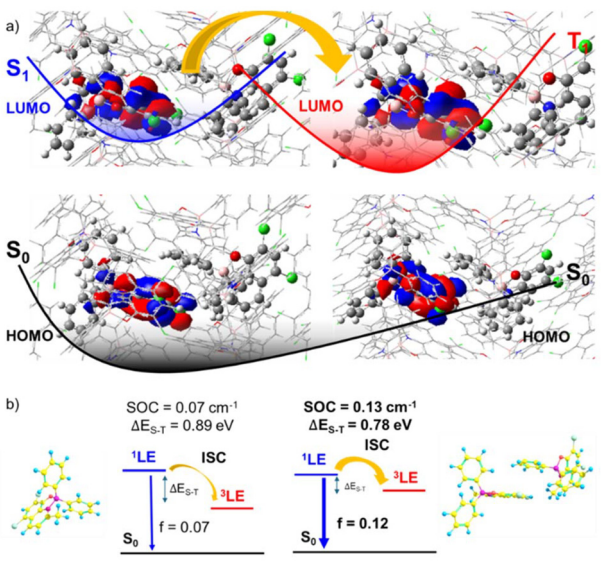

Fig. 4 (a) HOMO and LUMO images of the **BQ7** dimer at optimized S_1 and T_1 geometries, through QM/MM simulation; (b) illustration of the ISC process and fluorescence emission of **BQ7** in monomeric and dimeric forms along with SOC and energy gap between S_1 and T_1 states.

Fluorescence sensing of BQ7 in living cells

Encouraged by the intriguing photophysical properties of **BQ7** as a potential photosensitizer and fluorescence sensor, we sought to evaluate its feasibility within biological systems. Initially, we assessed the fluorescence of **BQ7** within living cells. Time-series imaging was conducted on live HeLa cells in a live cell chamber following the addition of **BQ7** at a concentration of 100 μM (Fig. 5a). The fluorescence of **BQ7** became detectable approximately 5 minutes post-treatment, reaching saturation at 10 minutes post-treatment. These results indicate that **BQ7** successfully diffuses across cellular membranes, with its fluorescence persisting within living cells. Notably, the fluorescence pattern of **BQ7** was not uniformly diffused throughout the cell (Fig. 5). Instead, it appeared to accumulate in certain membranous compartments, prompting us to investigate the specific intracellular organelles targeted by **BQ7**, which could also suggest its potential therapeutic functions.

We first examined lysosomes and mitochondria in live HeLa cells. The cells were incubated with 50 μM LysoTracker Deep Red or 100 μM MitoTracker Deep Red, along with 100 μM **BQ7**. However, confocal laser scanning microscopy (CLSM) imaging revealed a lack of colocalization of **BQ7** with either lysosomes or mitochondria (Fig. 5b). Based on the predicted hydrophobicity of **BQ7**, the vesicular structure, and the high refractivity observed in brightfield images, we hypothesized that **BQ7** accumulates in lipid droplets. To test this, we stained live HeLa cells with BODIPY 493/503 dye, which specifically stains neutral lipids and exhibits enhanced signals in lipid droplets. CLSM imaging of these samples demonstrated complete overlap between the signals of **BQ7** and BODIPY 493/503.

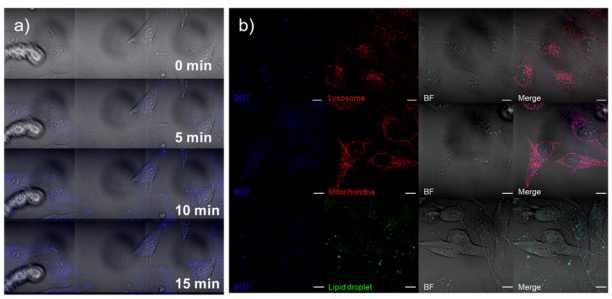

Fig. 5 (a) Fluorescence images of **BQ7** after incubation in living cells (0–15 min); (b) subcellular localization of **BQ7** (scale bar: 10 μm). BF: brightfield.

This journal is © The Royal Society of Chemistry 2026

Open Access Article. Published on 08 January 2026. Downloaded on 6/2/2026 4:10:33 PM.
This article is licensed under a Creative Commons Attribution 3.0 Unported Licence.

The calculated Pearson colocalization coefficient was 0.5299 for **BQ7** and BODIPY 493/503 (n = 4), compared to −0.0136 and 0.0004 for MitoTracker Deep Red (n = 3) and LysoTracker Deep Red (n = 4), respectively.

Therefore, we concluded that **BQ7** predominantly colocalizes with lipid droplets inside cells, rather than associating significantly with mitochondria or lysosomes. This specific accumulation in lipid droplets underscores the unique intracellular targeting properties of **BQ7**, suggesting its potential application in cellular imaging and targeted therapy.

Subsequently, we investigated the feasibility of Cu^{2+}-sensing by **BQ7** in live cell systems. HeLa cells were initially stained with 100 μM **BQ7**. Following complete staining, $CuCl_2$ was introduced to the cells in cell growth medium (DMEM with 10% FBS) at a final concentration of 100 μM. A dramatic decrease in **BQ7** fluorescence was observed 5–10 minutes post-treatment, culminating in an almost complete loss of fluorescence (Fig. 6). These findings unequivocally demonstrate the ability of **BQ7** to sense Cu^{2+} in live cells. We infer that the fluorescence quenching of **BQ7** is attributable to the formation of non-emissive **(Q7)$_2$Cu** complexes. Coupled with the colocalization results, we propose that **BQ7** can detect Cu^{2+} cations within lipid droplets.

Light-activated photocytotoxicity of BQ7 in living cells

In the previous experiment, we noted the morphological damage in the **BQ7** plus irradiation group, along with the delayed increase in ROS. Therefore, it is natural for us to study the cytotoxicity of **BQ7** under PDT conditions. HeLa cells were subjected to a dose-dependent cell viability test (**BQ7** concentrations of 0–100 μM), with or without light irradiation (Fig. 8). Under normoxic conditions, the HeLa cells showed a dose-dependent decrease in viability measured by CCK8 and spectrophotometry. It was notable that 100 μM **BQ7** with light irradiation showed a dramatic decrease 24 hours after irradiation, while the groups without light irradiation maintained their viability even at the highest concentration. Under hypoxic conditions, similar results were observed: 100 μM **BQ7** with light irradiation induced cell toxicity 24 hours after irradiation, while the groups without light irradiation remained unaffected. Additionally, we observed an almost complete lack of living cells in the 100 μM **BQ7** group at 48 hours after irradiation, while the cells were still viable in the light-unirradiated group at the same time point. Here, we could conclude that **BQ7** can induce photo-cytotoxicity under both normoxic and hypoxic conditions, demonstrating its potential for PDT applications.

Next, we investigated the cause of **BQ7**-mediated cell damage, along with the mechanism of the delayed ROS increase. Live HeLa cells were immediately stained with BODIPY 581/591 (a lipid-specific peroxidation dye) after **BQ7** treatment with or without light irradiation. CLSM imaging and quantitative analysis showed that the green to red fluorescence ratio in the lipid droplets increased in the light irradiation group, which indicates the peroxidation of the lipid at these locations (Fig. 9). On the other hand, the global green to red fluorescence was not different among the groups. The delayed ROS elevation observed in Fig. 7 might be a consequence of lipid peroxidation, the detailed mechanism of which will need further investigation.

We also observed delayed mitochondrial fission and swelling, which is evidence of mitochondrial damage, 180 minutes after PDT treatment with **BQ7**. At the same time, until 180 minutes, we could not observe any evidence of apoptotic cell death, including apoptotic bodies, nuclear fragmentation or DNA condensation. The morphological changes resemble those of ferroptosis.[20] These results suggest that the PDT treatment with **BQ7** leads to lipid droplet-specific peroxidation,

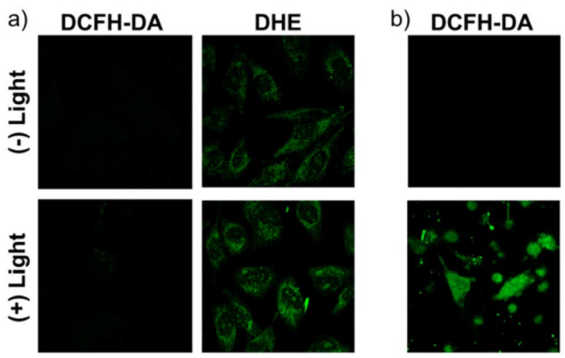

Fig. 7 Fluorescence images of (a) DCFH-DA and DHE, and (b) delayed measurement of DCFH-DA.

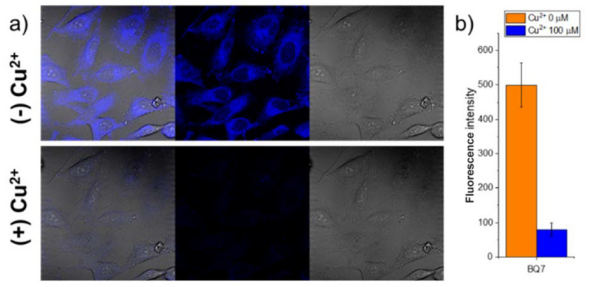

Fig. 6 (a) Fluorescence images of **BQ7** before and after treatment with Cu^{2+} in HeLa cells; (b) fluorescence intensity of **BQ7** before and after treatment with Cu^{2+} in HeLa cells.

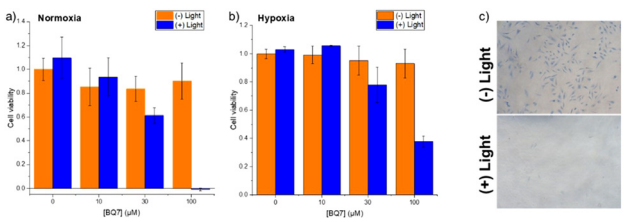

Fig. 8 Cell viability in the presence of **BQ7** with and without light irradiation under (a) normoxic and (b) hypoxic conditions at 24 h. (c) Brightfield image of cells at 48 h.

Open Access Article. Published on 08 January 2026. Downloaded on 6/2/2026 4:10:33 PM.
This article is licensed under a Creative Commons Attribution 3.0 Unported Licence.

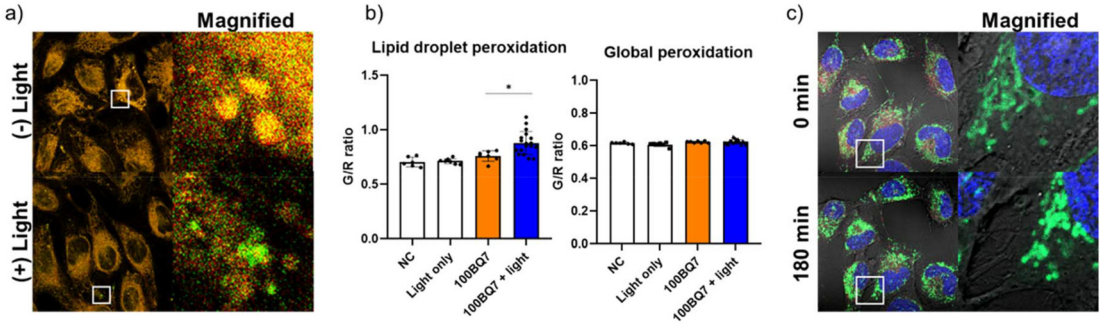

Fig. 9 Fluorescence images of (a) peroxidation of lipid droplets measured by BODIPY 581/591 and (b) quantitation of relative lipid droplet peroxidation. (c) Fluorescence image of **BQ7** under the treatment of PDT showing nuclei and mitochondria at 0 and 180 min.

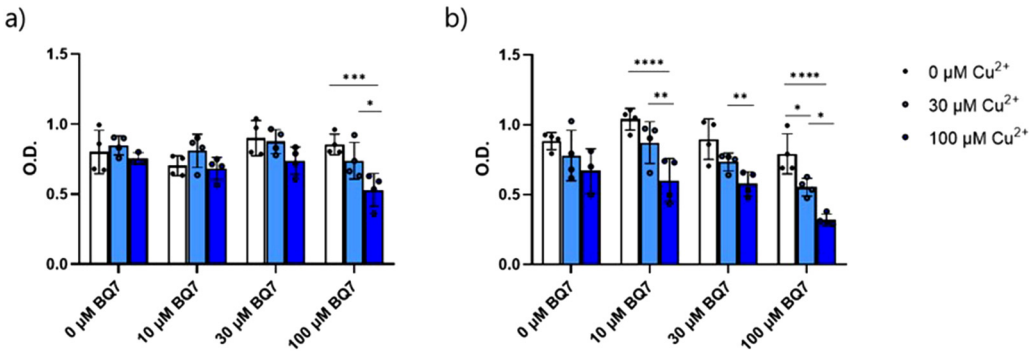

Fig. 10 Cell viability in the presence of **BQ7** (0–100 μM) and Cu^{2+} (0–100 μM) with (a) and without (b) light irradiation.

which is in accordance with the intracellular location of **BQ7**, leading to ferroptosis-like cell death.

Cu^{2+}-mediated (photo)cytotoxicity of BQ7 in living cells

In relation to the ability of **BQ7** to react with Cu^{2+} and form **$(Q7)_2Cu$** complexes in live cells. Cu complexes of quinoline showed cytotoxicity toward cancer cells.[26] We performed a CCK8 viability assay after treatment with 100 μM **BQ7** and 100 μM $CuCl_2$ with or without light irradiation. The HeLa cells were treated with **BQ7** in DMEM for 30 min. After a DPBS wash, $CuCl_2$ in DMEM was applied for 10 min. After another DPBS wash, the samples were irradiated. We found a significant Cu^{2+} dose-dependent decrease in cell viability in most of the groups tested with a greater impact in the light-irradiated groups (Fig. 10). Among the 100 μM $CuCl_2$-treated groups, the 100 μM **BQ7** group with light irradiation exhibited the highest cytotoxicity. Therefore, we can conclude that the presence of Cu^{2+} can enhance the photo- and dark-cytotoxicity of **BQ7** cancer cells, highlighting its potential for Cu^{2+}-mediated PDT and CMT applications.

Conclusion

In summary, a series of 8-hydroxyquinoline-based boron PSs (**BQ1–BQ7**) was synthesized, exhibiting intense fluorescence emission in solvents, films, solid states, and organic glass matrices. The $^1O_2$ QYs of the **BQ** series were enhanced by the presence of heavy atoms, such as iodine and bromine. However, the heavy-metal-free **BQ7** PS demonstrated efficient fluorescence emission and ROS generation through both type I and type II mechanisms in the aggregated state. QM/MM simulations revealed an increase in the oscillator strength of the S_1 state and the ISC process between the S_1 and T_1 states in the dimer form of **BQ7** as compared to its monomer form. Furthermore, **BQ7** showed the ability to detect Cu^{2+} ions *via* an on–off fluorescence emission in aggregates and within lipid droplets. PDT treatment with **BQ7** under both normoxic and hypoxic conditions resulted in lipid droplet-specific peroxidation, consistent with its intracellular localization, leading to ferroptosis-like cell death. Additionally, the treatment with Cu^{2+} enhanced the cytotoxicity of **BQ7**, suggesting a novel molecular design strategy for heavy-metal-free type I PSs aimed at ferroptosis-mediated PDT and chemotherapy.

Conflicts of interest

There are no conflicts to declare.

This journal is © The Royal Society of Chemistry 2026

Open Access Article. Published on 08 January 2026. Downloaded on 6/2/2026 4:10:33 PM. This article is licensed under a Creative Commons Attribution 3.0 Unported Licence.

Data availability

The data supporting this article have been included as part of the supplementary information (SI). Supplementary information: experimental and characterization data include NMR spectra, crystallographic data, photophysical measurements, biological experiments, and computational investigations. See DOI: https://doi.org/10.1039/d5dt01016k.

Acknowledgements

This work was sponsored by the NAFOSTED – FWO program with project numbers FWO.104.2020.03 and G0E5321N in Vietnam and the Flemish region, respectively. L. V. M. thanks the Hercules Foundation for supporting the purchase of the diffractometer through project AKUL/09/0035. The authors thank Prof. So Yeong Lee, Dr Flip de Jong, and Dr Jonathan Vandenwijngaerden for their valuable support in doing experiments. The authors thank Prof. Tan Le Hoang Doan for performing elemental analysis using the Euro Vector Elemental Analyser EA3100 Series at the Advanced Materials Technology Institute, Vietnam National University Ho Chi Minh City (VNUHCM-AMTI).

References

1 A. P. Castano, P. Mroz and M. R. Hamblin, *Nat. Rev. Cancer*, 2006, **6**, 535–545.
2 J. F. Lovell, T. W. B. Liu, J. Chen and G. Zheng, *Chem. Rev.*, 2010, **110**, 2839–2857.
3 X. Li, J. F. Lovell, J. Yoon and X. Chen, *Nat. Rev. Clin. Oncol.*, 2020, **17**, 657–674.
4 S. S. Lucky, K. C. Soo and Y. Zhang, *Chem. Rev.*, 2015, **115**, 1990–2042.
5 Z. Zhou, K. Ni, H. Deng and X. Chen, *Adv. Drug Delivery Rev.*, 2020, **158**, 73–90.
6 Y. Hong, J. W. Y. Lam and B. Z. Tang, *Chem. Soc. Rev.*, 2011, **40**, 5361–5388.
7 J. Zhang, S. Mukamel and J. Jiang, *J. Phys. Chem. B*, 2020, **124**, 2238–2244.
8 G. Feng, G.-Q. Zhang and D. Ding, *Chem. Soc. Rev.*, 2020, **49**, 8179–8234.
9 T. C. Pham, T. T. H. Hoang, D. N. Tran, G. Kim, T. V. Nguyen, T. V. Pham, S. Nandanwar, D. L. Tran, M. Park and S. Lee, *ACS Appl. Mater. Interfaces*, 2023, **15**, 47969–47977.
10 T. C. Pham, V.-N. Nguyen, Y. Choi, S. Lee and J. Yoon, *Chem. Rev.*, 2021, **121**, 13454–13619.
11 W. Fan, P. Huang and X. Chen, *Chem. Soc. Rev.*, 2016, **45**, 6488–6519.
12 B. M. Luby, C. D. Walsh and G. Zheng, *Angew. Chem., Int. Ed.*, 2019, **58**, 2558–2569.
13 Z. Zhou, J. Song, L. Nie and X. Chen, *Chem. Soc. Rev.*, 2016, **45**, 6597–6626.
14 J. M. Brown and W. R. Wilson, *Nat. Rev. Cancer*, 2004, **4**, 437–447.
15 A. Sharma, J. F. Arambula, S. Koo, R. Kumar, H. Singh, J. L. Sessler and J. S. Kim, *Chem. Soc. Rev.*, 2019, **48**, 771–813.
16 R. Wang, X. Li and J. Yoon, *ACS Appl. Mater. Interfaces*, 2021, **13**, 19543–19571.
17 L. Flamant, A. Notte, N. Ninane, M. Raes and C. Michiels, *Mol. Cancer*, 2010, **9**, 191.
18 J. Liu, C. Chen, T. Wei, O. Gayet, C. Loncle, L. Borge, N. Dusetti, X. Ma, D. Marson, E. Laurini, S. Pricl, Z. Gu, J. Iovanna, L. Peng and X.-J. Liang, *Exploration*, 2021, **1**, 21–34.
19 J. P. F. Angeli, R. Shah, D. A. Pratt and M. Conrad, *Trends Pharmacol. Sci.*, 2017, **38**, 489–498.
20 J. Ju, Y.-n. Song and K. Wang, *Aging Dis.*, 2021, **12**, 261–276.
21 M. Liu, B. Liu, Q. Liu, K. Du, Z. Wang and N. He, *Coord. Chem. Rev.*, 2019, **382**, 160–180.
22 J. Han, H. Kang, X. Li, N. Kwon, H. Li, S. Park and J. Yoon, *ACS Appl. Nano Mater.*, 2021, **4**, 5954–5962.
23 Y. Wen, H. Chen, L. Zhang, M. Wu, F. Zhang, D. Yang, J. Shen and J. Chen, *Free Radicals Biol. Med.*, 2021, **173**, 41–51.
24 J. Yang, X. Jin, Z. Cheng, H. Zhou, L. Gao, D. Jiang, X. Jie, Y. Ma and W. Chen, *ACS Sustainable Chem. Eng.*, 2021, **9**, 13206–13214.
25 W. S. Yang and B. R. Stockwell, *Trends Cell Biol.*, 2016, **26**, 165–176.
26 S. Tardito, A. Barilli, I. Bassanetti, M. Tegoni, O. Bussolati, R. Franchi-Gazzola, C. Mucchino and L. Marchiò, *J. Med. Chem.*, 2012, **55**, 10448–10459.
27 Y. Li, H. Zhou, S. Yin, H. Jiang, N. Niu, H. Huang, S. A. Shahzad and C. Yu, *Sens. Actuators, B*, 2016, **235**, 33–38.
28 L. Wang, Z.-L. Wei, Z.-Z. Chen, C. Liu, W.-K. Dong and Y.-J. Ding, *Microchem. J.*, 2020, **155**, 104801.
29 G. Zhang, Y. Li, J. Xu, C. Zhang, S. Shuang, C. Dong and M. M. Choi, *Sens. Actuators, B*, 2013, **183**, 583–588.
30 S. Wu, X. Ma, Y. Wang, J. Zhou, X. Li and X. Wang, *Spectrochim. Acta, Part A*, 2021, **249**, 119330.
31 L. Zhang, J. Sun, S. Liu, X. Cui, W. Li and J. Fang, *Inorg. Chem. Commun.*, 2013, **35**, 311–314.
32 Z. Han, D. Nan, H. Yang, Q. Sun, S. Pan, H. Liu and X. Hu, *Sens. Actuators, B*, 2019, **298**, 126842.
33 M. Li, L.-C. Feng, S.-S. Feng and W.-K. Dong, *J. Mol. Struct.*, 2022, **1261**, 132926.
34 W. Qin, M. Baruah, M. Van der Auweraer, F. C. De Schryver and N. Boens, *J. Phys. Chem. A*, 2005, **109**, 7371–7384.
35 W. Kohn, A. D. Becke and R. G. Parr, *J. Phys. Chem.*, 1996, **100**, 12974–12980.
36 C. Adamo and D. Jacquemin, *Chem. Soc. Rev.*, 2013, **42**, 845–856.
37 S. Hirata and M. Head-Gordon, *Chem. Phys. Lett.*, 1999, **314**, 291–299.
38 A. M. May and J. L. Dempsey, *Chem. Sci.*, 2024, **15**, 6661–6678.

39 M. V. Veidis, G. H. Schreiber, T. E. Gough and G. J. Palenik, *J. Am. Chem. Soc.*, 1969, **91**, 1859–1860.
40 M. A. Halcrow, *Chem. Soc. Rev.*, 2013, **42**, 1784–1795.
41 J. Wang, J. Ren, Q. Tang, X. Wang, Y. Wang, Y. Wang, Z. Du, W. Wang, L. Huang, L. A. Belfiore and J. Tang, *Materials*, 2022, **15**, 1719.
42 C. M. Marian, *Wiley Interdiscip. Rev.:Comput. Mol. Sci.*, 2012, **2**, 187–203.
43 T. J. Penfold, E. Gindensperger, C. Daniel and C. M. Marian, *Chem. Rev.*, 2018, **118**, 6975–7025.
44 A. Baiardi, J. Bloino and V. Barone, *J. Chem. Phys.*, 2014, **141**, 114108.
45 L. W. Chung, W. M. C. Sameera, R. Ramozzi, A. J. Page, M. Hatanaka, G. P. Petrova, T. V. Harris, X. Li, Z. Ke, F. Liu, H.-B. Li, L. Ding and K. Morokuma, *Chem. Rev.*, 2015, **115**, 5678–5796.

Open Access Article. Published on 08 January 2026. Downloaded on 6/2/2026 4:10:33 PM.
This article is licensed under a Creative Commons Attribution 3.0 Unported Licence.

This journal is © The Royal Society of Chemistry 2026